

Transmon Architecture for Emission and Detection of Single Microwave Photons

Daniel L. Campbell,^{1,*} Stephen McCoy,² Melinda Andrews,² Alexander Madden,² Viva R. Horowitz,³ Bakir Husremović,³ Samuel Marash,³ Christopher Nadeau,² Man Nguyen,² Michael Senatore,¹ Samuel Schwab,¹ Erin Sheridan,¹ and Matthew D. LaHaye^{1,†}

¹*Air Force Research Laboratory, Information Directorate, Rome NY 13441 USA*

²*Booz Allen Hamilton, McLean, VA USA 22012*

³*Physics Department, Hamilton College, Clinton NY 13323 USA*

(Dated: January 19, 2026)

We showcase the recently developed double transmon coupler (DTC) circuit as a compact, drop-in, tunable and transition-selective link between an otherwise coherent transmon and the continuum of modes in a waveguide. We use these transmon-DTC devices as transmon emitter/dectectors (TEDs) for microwave photons. We highlight the flexibility of these devices by sending photons from a source TED to a measurement TED using a meter of coaxial cable and a circulator, each TED with nominally identical circuit parameters. We detect 60 % of the photons using this setup where we infer that 95 % of the photons at the input of the measurement TED are detected. Reset and photon emission/detection each require about $2\ \mu\text{s}$, for a minimum protocol duration of $4\ \mu\text{s}$, for our choice of TED parameters. Transmon-waveguide links like the DTC serve an important role in quantum information processors: they provide a mechanism for unconditional fast reset, metrology, and as nascent quantum communication interfaces for quantum networking.

I. INTRODUCTION

Networking physically separate quantum processing units (QPUs) is an attractive approach for scaling quantum computers [1–4], enabling remote quantum computation, and leveraging quantum advantage in networks of distributed sensors [5]. Superconducting circuits can exhibit strong near-field interactions with one-dimensional waveguides, enabling the high fidelity creation [6–11], capture [12–17], and detection [18–27] of single microwave photons. These are essential functionalities of a quantum communication interface (QCI) architecture, analogous to classical serial network interfaces. An effective QCI for a transmon quantum computing architecture would ideally also be compact, operate programmably in both transmitter and receiver modes, support a broad range of microwave frequencies, provide isolation to prevent QPU decoherence, and allow for selective entanglement with the host QPU.

Here we demonstrate a compact, frequency tunable, and transmon compatible QCI, a transmon emitter/detector (TED). The TED mediates time-dependent interactions between a well-isolated long-lived transmon qubit memory and the modes of a coplanar waveguide. As we highlight in this paper, the versatile TED circuit can be used to release, capture, and detect itinerant microwave photons. In this work we showcase two TED devices indexed $x \in \{s, m\}$: one to source ‘ s ’ and the other to measure ‘ m ’ microwave photons (Fig. 1).

The TED expands on the recently developed double transmon coupler (DTC) [28–31] architecture, developed independently by Toshiba and the Air Force Research

Laboratory (AFRL). The DTC consists of two transmons, Q_{cx} and Q_{wx} , linked by an inductive Josephson junction. The TED adds a third “data” transmon Q_{dx} which is capacitively coupled to Q_{cx} , as shown in Fig. 1a-b. This setup isolates Q_{dx} from the waveguide environment, which is strongly coupled to Q_{wx} located on the other side of the DTC. (See Appendix A for chip fabrication information.)

The frequency of Q_{wx} then sets the energy of photons emitted/detected by the TED, while the relaxation rate γ_x of Q_{wx} to the waveguide sets the maximum TED bandwidth. Modulating the DTC flux hybridizes Q_{wx} and Q_{dx} , operating the TED, while Q_{cx} is far off resonance. In a different context, a DTC was used to demonstrate a high fidelity controlled-Z gate between two data transmons [30], where the DTC passively suppressed spurious $\sigma_z\sigma_z$ interactions between data transmons in the DTC’s off configuration.

The frequencies and coupling of transmons Q_{cx} and Q_{wx} tune approximately equally in magnitude with flux applied to the DTC’s superconducting quantum interference device (SQUID), analytically described in Ref. [28] and illustrated in Fig 1c. Q_{dx} ’s lifetime is independent of the DTC flux and protected from the waveguide if Q_{dx} ’s frequency is sufficiently different from Q_{wx} ’s. Instead, static flux on the DTC primarily tunes Q_{wx} ’s frequency over a range of several hundred MHz, shown in Fig. 1c. An exchange interaction between Q_{dx} and the waveguide is then readily established by resonantly driving the DTC flux at the difference or sum of Q_{dx} and Q_{wx} ’s frequencies.

The several hundred MHz usable frequency tuning range for the TED-waveguide interactions relaxes parameter setting requirements for entanglement distribution between chips and other heterogeneous components. Similarly, the static frequency of Q_d is compatible with the restrictive frequency setting requirements of most

* Daniel.Campbell.22@us.af.mil

† Matthew.LaHaye@us.af.mil

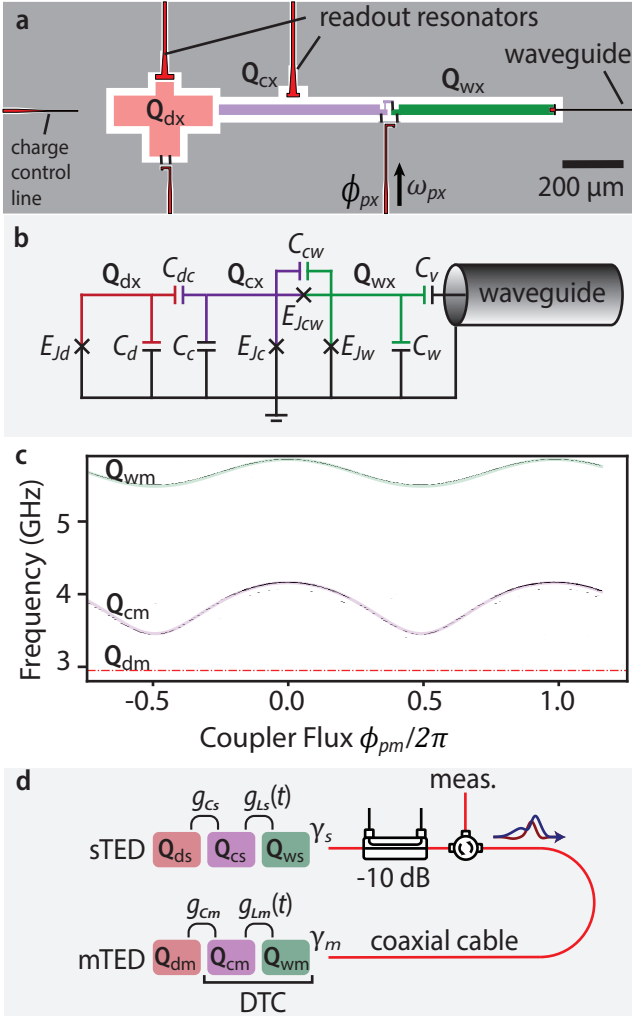


FIG. 1. (a) CAD file illustrating the transmon emitter/detector (TED) layout and (b) equivalent circuit for the TED where we index between two TEDs: $x \in \{s, m\}$. Transmon Q_{dx} (red) is designed for long term storage while Q_{wx} (green) strongly couples to a waveguide. Q_{cx} (purple) and Q_{wx} comprise a double transmon coupler (DTC). Flux line ϕ_{px} biases and sinusoidally drives the DTC to mediate interactions between Q_{dx} and Q_{wx} . (c) Flux tunability with ϕ_{pm} of the measurement TED's (mTED's) Q_{cm} and Q_{wm} transitions. Q_{wm} was measured using backscatter while Q_{cm} was measured using two-tone spectroscopy. The red dash-dot line is a guide to the eye showing Q_{dm} 's transition, which only varies on the ~ 10 MHz scale. (d) Depiction of emission-detection setup. A source TED (sTED) is connected to the mTED via 1 meter of coaxial cable, a 10 dB directional coupler, and a circulator. The coupler and circulator allow backscatter measurements of Q_{wx} , which does not have an independent read-out resonator. Q_{dx} and Q_{cx} are capacitively coupled with amplitude g_{Cx} while Q_{cx} and Q_{wx} are inductively coupled with amplitude g_{Lx} . γ_x is the rate Q_{wx} relaxes into its waveguide.

transmon QPUs. This work and Ref. [22] both create and detect a Fock state. Sources, receivers, and detectors that use cavities have limited waveguide frequency tunability [6, 8, 17, 23, 24, 26, 32]. Other architectures have similar waveguide tunability while requiring Q_d and Q_w to have similar frequencies [7, 11, 16, 33] or are not based on a transmon architecture [18, 20, 25, 27]. It is unclear whether Ref. [7] and its successors can operate with Q_d and Q_w separated by multiple gigahertz in frequency. This separation is not only possible, but preferable, with a TED.

To highlight the flexibility of the TED circuit we use TEDs with identical circuit parameters, operated differently, for a pitch-detect demonstration between remote transmons. One TED acts as a single microwave photon Fock source, and a second TED acts as a windowed classical microwave photon detector for that source. The two chips are linked by a coaxial cable interrupted by a circulator. The circulator enforces a continuum of modes in the waveguide and retrieves the outgoing waveform as shown in Fig. 1a-d. We then compare the operation of the windowed microwave photon detector under Fock state versus coherent state illumination. This paper is structured to first introduce the TED theory of operation and then discuss the operation of the TED as a microwave photon source and detector. Finally, we put together all of the components for the Fock-state emission and detection demonstration and discuss the results.

II. THEORY OF OPERATION

TED transmons have distinct roles based on their position in the circuit: we use indices $q \in \{d, c, w\}$ so that Q_{dx} , Q_{cx} , and Q_{wx} label the data, coupling, and waveguide transmons, respectively. We similarly label the lowering operator d_x , c_x , and w_x for transmons Q_{dx} , Q_{cx} , and Q_{wx} , respectively. Q_{dx} and Q_{cx} are capacitively coupled with magnitude g_{Cx} , as labeled in Fig. 1d. The coupling between Q_{cx} and Q_{wx} is a combination of inductive g_{Lx} and capacitive, where we neglect the capacitive part because it does not play a role in the driven dynamics. The dimensionless flux parameter $\phi_{px}(t) = \bar{\phi}_{px} + A_{\phi x} \sin(\omega_{px}t)$ acts on the DTC where changing ϕ_{px} by 2π returns the DTC to its original configuration, corresponding to the flux quantum. We write an effective form for the inductive coupling $g_{Lx}(t) \sim g_{L0x} \cos(\bar{\phi}_{px} + A_{\phi x} \sin(\omega_{px}t)) \approx \bar{g}_{Lx} - A_x \sin(\omega_{px}t)$ where $\bar{g}_{Lx} = g_{L0x} \cos(\bar{\phi}_{px})$ and $A_x \approx A_{\phi x} \sin(\bar{\phi}_{px})$: the exact functional form can be derived from Ref. [28]. We introduce a simplified state-space description of the TED that is coherently driven through its waveguide (see Appendix B). The density matrix ρ satisfies the effective master equation

$$\dot{\rho}_x = -\frac{i}{\hbar} [H_x, \rho_x] + \gamma_x \mathcal{L}[w_x] \rho_x \quad (1)$$

where \mathcal{L} is the Lindblad dissipator and the Hamiltonian takes the form

$$\begin{aligned} \frac{H_x}{\hbar} = & \sum_{q=d,c,w} \omega_{qx} q_x^\dagger q_x + \nu_{qx} q_x^\dagger q_x^2 \\ & + \left[g_{Cx} (d_x^\dagger c_x + d_x c_x^\dagger) - g_{Lx}(t) (c_x^\dagger w_x + c_x w_x^\dagger) \right. \\ & \left. - i\Omega_x(t) \sin(\omega_{\alpha x} t) (w_x - w_x^\dagger) \right]. \end{aligned} \quad (2)$$

ν_{qx} is the anharmonicity and ω_{qx} is the frequency of each Q_{qx} . The first line of Eq. (2) represents the anharmonic oscillator level structure of the three transmons in the TED. The second line describes effective transmon-transmon interactions within a TED. We include the last term to illustrate the response of Q_w to a coherent drive that we apply to characterize and calibrate the TED in detection mode, where $\Omega_x(t)$ is the instantaneous Rabi rate. Note, that $\Omega_x = 0$ in the emission/detection demonstration. g_{Lx} , ω_{qx} , and neglected terms proportional to q_x and q_x^\dagger will oscillate in response to a time varying ϕ_{px} with amplitude $A_{\phi x}$. These oscillations produce the desired parametric driving term, frequency shifts that scale with $A_{\phi x}$, and effective Rabi drives, respectively. Therefore, we must carefully set the frequencies of Q_{dx} , Q_{cx} , and Q_{wx} to avoid unwanted Rabi transitions.

The lifetimes of Q_{dx} and Q_{cx} should not be inferred from master equation simulations of Eq. (1) [34], or the traditional Purcell formula derived using assumptions valid in atomic physics, see the supplement of Ref. [35]. Neither approach is suitable when qubit-qubit detuning is similar in magnitude to qubit frequencies. Instead, the lifetime of Q_{dx} can be perturbatively estimated using a RC time-constant approach [36, 37], which is accurate when the coupling between Q_{dx} and Q_{cx} is in the dispersive regime ($|g_{Cx}|/|\omega_{dx} - \omega_{cx}| < 0.1$) and $\omega_{dx} \neq \omega_{wx}$. Under these conditions the relaxation rate of Q_d is

$$\Gamma \approx \frac{\text{Re}(Y)}{C_d + C_{dc}} \quad (3)$$

where Y is the admittance of the node associated with Q_{dx} (Fig. 1b) to ground when the coax cable is replaced with a 50Ω resistor to ground. We write out Y for Q_{dx} in Appendix E. In general, it is easiest to make Q_{dx} long-lived over the full range of ϕ_{px} when $\omega_{dx} < \omega_{wx}$. For the circuit parameters studied here, we estimate that the waveguide limits $Q_{dx} T_1 < 13\text{ ms}$ at $\phi_{px} = 0$, for which \bar{g}_{Lx} is large.

For the experiments reported here, the time dependence of $g_{Lx}(t)$, $A_x(t)$, is established by modulating ϕ_{px} at $\omega_{px} = |\omega_{wx} - \omega_{dx}|$. Additionally, for detector TED characterization and calibration, the coherent drive Ω_x is applied at frequency $\omega_{\alpha x} \sim \omega_{wx}$. To model these time dependencies, we apply two independent rotating-wave transformations while neglecting counter-rotating terms, thus obtaining a stationary form for Eq. (2) (see Appendix C for details of the derivation). In the new basis, we use perturbation theory to eliminate Q_{cx} , where

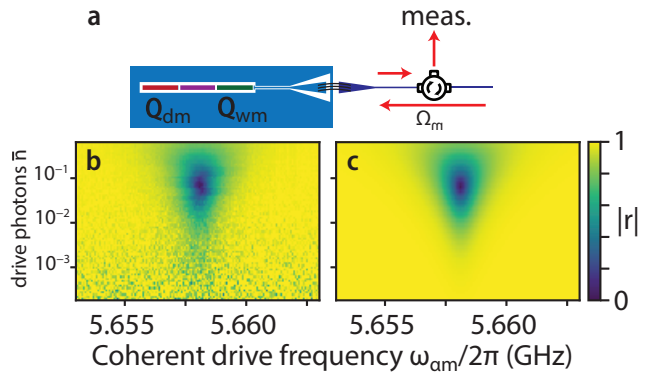


FIG. 2. (a) Layout of mTED, where a coherent drive is applied to Q_{wm} . (b-c) Calibration of coherent drive power using a vector network analyzer measurement of Q_{wm} illuminated when $g_{pm} = 0$. $|r|$ is the normalized amplitude of the returning coherent state. The plots vary coherent drive frequency and power.

we assume Q_{cx} is far off resonance and never deliberately excited. The resultant effective coupling between Q_{dx} and Q_{wx} is $g_{px} = g_{Cx} A_x(t) / 2(\omega_{dx} - \omega_{cx})$ (see Appendix C 1), where modulating $A_x(t)$ and hence $g_{px}(t)$ enables TED operation. We can now represent the TED state as $|n_{dx} n_{wx}\rangle$, where n_{dx} and n_{wx} represent excitations on Q_{dx} and Q_{wx} , respectively. We write down the approximate stationary TED Hamiltonian

$$\begin{aligned} \frac{H_{\text{RWA}x}}{\hbar} = & \left[(\delta_x - \delta_{px}) d_x^\dagger d_x + \delta_x w_x^\dagger w_x + \Omega_x(t) (w_x + w_x^\dagger) / 2 \right. \\ & + \nu_{dx} d_x^\dagger d_x^2 + \nu_{wx} w_x^\dagger w_x^2 \\ & \left. - i g_{px}(t) (d_x^\dagger w_x - d_x w_x^\dagger) \right]. \end{aligned} \quad (4)$$

where $\delta_x = \omega_{wx} - \omega_{\alpha x}$ and $\delta_{px} = \omega_{wx} - \omega_{dx} \pm \omega_{px}$ is the detuning of the parametric drive from the $|10\rangle \leftrightarrow |01\rangle$ transition where we choose the sign that minimizes the magnitude of δ_{px} . This transition hybridizes Q_{dx} and Q_{wx} and can be used to reset Q_{dx} . To initialize each TED we perform a reset and then excite Q_{dx} . We neglected the term required to Rabi Q_{dx} from Eq. 4 for brevity.

A. Device characterization

Measuring the backscatter of a coherent state from Q_w , Fig. 2a-c, allows for the convenient measurement of the properties of a TED. Q_{wx} has a nonlinear amplitude-dependent response to the coherent drive that can be divided into three distinct scattering regimes, ordered by increasing incident drive power: elastic, inelastic, and saturated. The elastic regime corresponds to drive powers that would be too weak to excite an equivalent linewidth harmonic oscillator from its ground state to its second excited state. Q_{wx} 's two-state system then interacts with the drive as if it were a harmonic oscillator. A harmonic oscillator illuminated by a coherent

drive emits with π additional phase and twice the amplitude. We sum this emission with the reflected drive to obtain the return signal, which has the same amplitude as the input signal. Thermal occupation of the waveguide and hence Q_{wx} re-introduces non-linearity, reducing the coherent amplitude emitted by Q_{wx} . Similarly, as the drive power increases, in the intermediate regime, the coherent amplitude emitted by Q_{wx} also decreases. According to our model (Fig. 2), at $P = \hbar\omega_{wx}\gamma_x/16$ the reflected drive and Q_{wx} destructively interfere. On a vector network analyzer the returning signal shows a dip because it has no coherent amplitude. The saturated regime corresponds to stronger input drives where the photon absorbed by the qubit is a negligible fraction of the total and where the coherent amplitude emitted by Q_{wx} is zero. In this regime the scattered response appears as it would if there was no qubit. Fitting to all three regimes can provide sensitive information about Q_{wx} such as the frequency $\omega_{wx}/2\pi = 5.65811(1)$ GHz, decay rate $\gamma_m = 11.2(1) \times 10^6$ s $^{-1}$, and thermal occupation $n_{th} = 0.015(3)$ of Q_{wx} . This measurement of n_{th} is consistent with the mode occupation of Q_{dm} measured after reset.

The anharmonicity of Q_{wx} is obtained by monitoring the reflected response of Q_{wx} in the elastic or intermediate power regime while scanning a second coherent drive in frequency. When the frequency of the second drive sweeps through $|01\rangle \leftrightarrow |02\rangle$, it reduces the response from the drive probing the $|00\rangle \leftrightarrow |01\rangle$ transition. The physics of this measurement is related to electromagnetically induced transparency [38]. The anharmonicity ν_{wx} is $-169(2)$ MHz.

We obtain the transition frequencies and anharmonicities of Q_{cx} and Q_{dx} with standard two-tone spectroscopy through the qubits' readout resonators [39] and report them in Table I. The lifetime and coherence of Q_{dx} is $T_1 = 81(35)$ μ s and $T_2 = 41(6)$ μ s, measured at their upper sweet spots, and independent of ϕ_{px} . We also found that T_1 and T_2 lifetimes were unchanged when the parametric drive $g_{px} = 0.584(6)\gamma_m$ was turned on for TED detection (so long as photons are not applied to Q_{wx}).

Fitting theory [28] to the experimentally measured DTC transmon frequencies as a function of flux, we infer the DTC coupling is $g_{L0} = (0.30(1)$ GHz) $\cos(\phi_p)$ at $\phi_{px} = 0$. From finite element simulations in ANSYS Q3D, the capacitive coupling between Q_{dx} and Q_{cx} is $g_{Cx}/2\pi \approx 70$ MHz.

III. SOURCE AND DETECTOR OPERATION

In subsections III A, III B, and III C, the source TED (sTED) and measurement TED (mTED) comprise a larger two-TED system (Fig. 1d). States in this larger system are represented as $|sTED\rangle \otimes |mTED\rangle$. We will use the notation $|sTED\rangle \otimes |\cdot\rangle$ and $|\cdot\rangle \otimes |mTED\rangle$ in situations where the state of the mTED and sTED, respectively, are unimportant to the discussion.

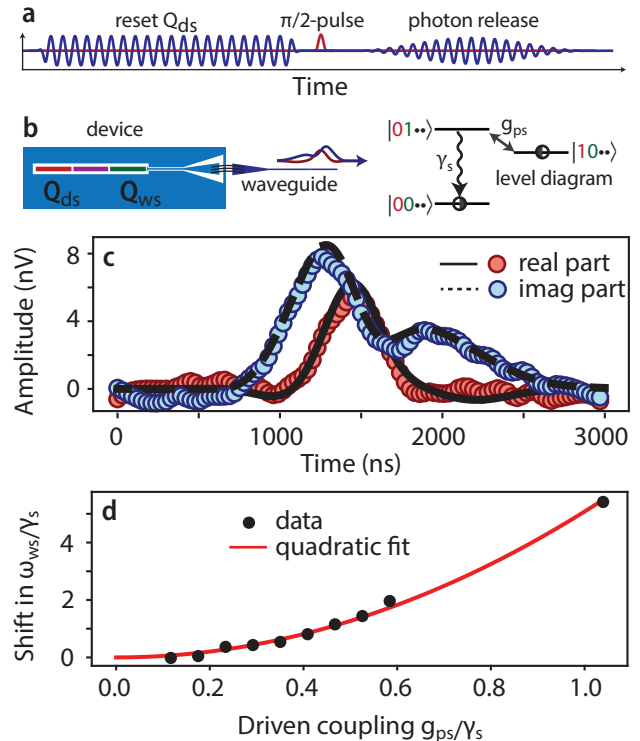


FIG. 3. (a) Pulse timing diagram for parametric coupling and qubit gates. A flux drive is initially applied to the sTED resonator with the $|10 \cdot \cdot \rangle \leftrightarrow |01 \cdot \cdot \rangle$ transition to reset the residual thermal population from Q_{ds} . Q_{ds} is then excited to $(|10 \cdot \cdot \rangle + |00 \cdot \cdot \rangle)/\sqrt{2}$ by a $\pi/2$ -pulse and subsequently driven by a shaped flux drive on the reset transition to release a photon state. (b) (left) Layout of sTED, where a photon emits into a 50Ω waveguide. (right) Level diagram with Q_{ds} prepared in a superposition state, depicted using half filled circles. g_{ps} is the amplitude of a drive on a transition that releases the state on Q_{ds} . γ_s is the relaxation rate of Q_{ws} into the waveguide. (c) Markers show the average of ten thousand repetitions of the photon superposition state after amplification. Error bars on the data are smaller than the marker size. The amplitude of the output was rescaled to match the theory fit (lines). The complex dynamics of the photon wavefunction result from a frequency shift of Q_{ws} with g_{ps}/γ_s . These shifts can be passively eliminated (see Appendix D) (d) Measured frequency shift in the ω_{ws} as a function of g_{ps}/γ_s where the marker size is roughly equivalent to the error and the line is a fit to a quadratic function.

A. Source operation

We perform the sequence of pulses shown in Fig. 3a-b to emit a Fock-vacuum superposition microwave photon from Q_{ds} into the waveguide. The energy of the emitted photon is controlled by selecting a static ϕ_{ps} that sets the desired ω_{ws} . A $\pi/2$ -pulse along the local charge line to Q_{ds} excites the sTED to $(|10 \cdot \cdot \rangle + |00 \cdot \cdot \rangle)/\sqrt{2}$. Subsequently, we drive the $|10 \cdot \cdot \rangle \leftrightarrow |01 \cdot \cdot \rangle$ transition by modulating g_{ps} . This hybridizes Q_{ds} with Q_{ws} , where Q_{ws} rapidly releases the excitation into the waveguide at

frequency ω_{ws} . This drive is also applied at the beginning of the sequence to reset Q_{ds} into its ground state.

Without a reset pulse, we measured Q_{ds} to have a 12% $|10..\rangle$ occupation. To mitigate this unwanted residual population, we use a $2\mu\text{s}$ parametric drive on the $|10..\rangle \leftrightarrow |01..\rangle$ transition, labeled “reset Q_{ds} ” in Fig. 3a, bringing Q_{ds} into equilibrium with the mode occupation of the waveguide at ω_{ws} . Q_{ds} is then measured to have 1.5% occupation of $|10..\rangle$. We performed this reset prior to each experimental repetition to improve state initialization fidelity and consistency.

The Fock-vacuum superposition state was routed through the amplifier chain (See Appendix I for description of the measurement circuit), demodulated, and averaged over ten thousand measurements on a digitizer, see Fig. 3c. The time and frequency dependence of an equivalent Fock state wavefunction, produced when Q_{ds} is fully excited during initialization, can be inferred from this averaged measurement [11, 40, 41].

Figure 3c shows the real and imaginary voltage components of the emitted wavefunction. We do not carefully shape the emitted wavefunction as other works have [8, 16] because the fidelity of photon detection by the mTED is not sensitive to the phase information (see Sec. III C). Instead, we applied $g_{ps} \propto A_s$ with the cosine shape

$$A_{\phi s}(t) = A_{\phi s} \sin(\bar{\phi}_{ps}) \cos^2\left(\frac{\pi(t - t_0)}{T}\right) \quad (5)$$

for $t - t_0 \in (-T/2, T/2)$ (as illustrated in Fig. 3a). We simulated and measured that, with duration $T = 2\mu\text{s}$, this shape is statistically likely to release a photon into the waveguide.

We measured that ω_{ws} shifts quadratically with applied g_{ps} , plotted in Fig. 3d, resulting in a non-linear phase evolution in Fig. 3c. The wavefunction phase has a linear slope with time when g_{ps} is constant. We fit to the wavefunction in Fig. 3c using Eq. 4. This simulation incorporates the frequency shift of Q_{ws} in Fig. 3d and let the amplitude of g_{ps} vary as a free parameter, finding $g_{ps}(t) = 0.472(2)\gamma_s$ at $t = t_0$. We also tried allowing the quadratic prefactor of the shift on ω_{ws} to vary as a free parameter and obtained a result consistent with Fig. 3d. There are two roughly co-equal origins to the shift. First, the off-resonant interaction of the modulating inductive coupling A_s with Q_{cs} induces an ac Stark shift of ω_{ws} equivalent to $A_s(t)^2/4(\omega_{ds} - \omega_{cs})$. Second, the dispersion of $\omega_{ws}(\phi_{ps})$ has some curvature about most bias points $\bar{\phi}_{ps}$, resulting in some rectification.

We subsequently measured a different TED with a larger g_{Cs} and E_{Jcws} where the shift was much less than γ_s when $g_{ps} \approx \gamma_s/2$, the value for g_{ps} that maximizes the relaxation rate of Q_{ds} . However, the Q_{ds} for this other TED had a shorter lifetime. We discuss in Appendix D how to optimize for both Q_{ds} coherence and small shifts.

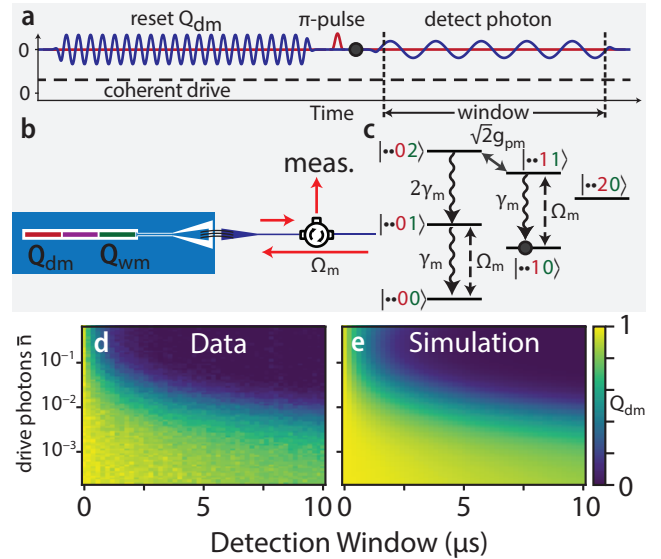


FIG. 4. (a) Pulse timing diagram for the mTED and an externally applied coherent drive (which is always on). The mTED is initialized using a reset pulse on the $| \cdot \cdot 10 \rangle \leftrightarrow | \cdot \cdot 01 \rangle$ transition followed by exciting Q_{dm} to $| \cdot \cdot 10 \rangle$ with a π -pulse. A parametric drive on the $| \cdot \cdot 11 \rangle \leftrightarrow | \cdot \cdot 02 \rangle$ transition turns on detection. (b) Layout of mTED, where a coherent drive is applied to Q_{wm} . (c) Level diagram indicating the driven transitions and relaxation pathways. g_p is the amplitude of a driven coupling while γ_m is the mTED’s relaxation of Q_{wm} into the waveguide. (d-e) Population of Q_{dm} as a function of duration g_p is applied and coherent drive power.

B. Detector operation

To preface this section, we need to distinguish microwave photon detection from waveguide mode capture: the capture protocol [12–17] swaps the quantum state (up to one photon) of a single waveguide mode with Q_{dm} . Q_{dm} may then be measured to detect single photons. Tomography on Q_{dm} can statistically determine the full quantum state of the waveguide mode. By contrast, microwave photon detection [18, 19, 21–26] integrates over all the modes of the waveguide within the detection window and bandwidth at the cost of measuring the photonic state. If a photon is present within the time window and bandwidth of the detector, Q_{dm} latches. At optical frequencies physical implementations of photon detectors include photomultiplier tubes and superconducting nanowire single photon detectors. Let’s consider measurements of waveguide modes with the Fock-vacuum superposition $(|1\rangle - |0\rangle)/\sqrt{2}$: using photon capture, the phase of the superposition could be inferred using tomography; whereas with photon detection, only the probability of obtaining a Fock state could be inferred.

In this work, we demonstrate a microwave photon detection technique that integrates over a temporal window with bandwidth γ_m about frequency ω_{wm} . Q_{dm} latches to its ground state with high probability if at least one excitation in the waveguide is present during

the integration window. The procedure begins with exciting the mTED into $|\cdot\cdot10\rangle$ using a π -pulse on Q_{dm} (black dot in Fig. 4a). We then apply a coherent drive along the waveguide (Fig. 4b): the coherent drive with amplitude Ω_m or any other source of photons will excite the system to $|\cdot\cdot10\rangle \rightarrow |\cdot\cdot11\rangle$ (Fig. 4c). We use the DTC flux line to drive the transition $|\cdot\cdot11\rangle \leftrightarrow |\cdot\cdot02\rangle$ at $\omega_{pm} = |\omega_{wm} - \omega_{dm}| + \nu_{wm}$ and with amplitude g_{pm} (Fig. 4c): the duration that this transition is driven corresponds to the mTED's detection window. In this manner, Q_{wm} will only reach the $|\cdot\cdot02\rangle$ if an incoming photon had first triggered excitation $|\cdot\cdot01\rangle \rightarrow |\cdot\cdot11\rangle$.

If the photon wavefunction arrives within the bandwidth and detection window of the mTED, the detection efficiency for that photon can be near unity. This is generally easiest to achieve by making $\gamma_m/2\pi$ much larger than the bandwidth of the photon and the detection window long enough to absorb the photon. The incident photon is absorbed and then re-emitted as a pair of correlated photons at ω_{wm} and $\omega_{wm} + \nu_{wm}$ [42] while the mTED relaxes rapidly $|\cdot\cdot02\rangle \rightarrow |\cdot\cdot00\rangle$. See Appendix G for more analysis of mTED operation. Since the mTED remains in $|\cdot\cdot10\rangle$ in the absence of a photon, measuring Q_{dm} after this procedure indicates the presence or absence of a photon detected from the waveguide. Relaxation of Q_{dm} during photon detection and readout corresponds to a false detection event (or dark count) using this protocol. We can expect $\sim 16\%$ false detection events with a $81(35)\mu\text{s}$ lifetime for Q_{dm} , a $10\mu\text{s}$ detection window, and $4\mu\text{s}$ readout duration. False detection events are undesirable for some quantum networking applications, such as entanglement heralding, via DLCZ [43] or Barrett-Kok [44] protocols, within which false detector click events contribute to infidelity in the generated remote Bell state.

We compared the behavior of the mTED to our model (Eq. 4 and Appendix H) with the amplitude of g_{pm} as a free parameter. Using the setup described in Fig. 4a-c, we monitored the population of Q_{dm} as a function of coherent drive power $\hbar\omega_{wm}\gamma_m\bar{n}$ applied along the waveguide at frequency ω_{wm} and the detection window (when $g_{pm} \neq 0$). Fitting simulation to data in Fig. 4d-e gives $g_{pm} = 0.259(3)\gamma_m$ for our initial choice of \bar{n} . Since $g_{pm} \propto \sqrt{\bar{n}}$ we can use this measurement to extrapolate the value of \bar{n} , and hence the coherent drive power, for which Fock and coherent detection efficiency is maximized: $g_{pm} \geq \gamma_m/2$. The choice of $g_{pm} = \gamma_m/2$ maximizes the detection bandwidth. The procedure for calibrating the coherent drive power outside the cryostat to \bar{n} is described in section II A.

C. Pitch-detect demonstration

We demonstrate Fock state detection by using the sTED to emit a microwave photon followed by detecting the microwave photon with the mTED. The two TEDs are connected via a meter of non-superconducting coaxial cable, a directional coupler, and a circulator, as depicted

in Figs. 1d and 5b. The circulator creates a continuum of modes, allowing an itinerant photon to be sent from the sTED to the mTED and anything emitted or reflected from the mTED to the measurement chain.

We model the sTED and mTED interacting through a circulator using the SLH framework [45–47]. We take the circulator and cabling to be lossy with loss strength parameter $\eta \in [0, 1]$. A density matrix ρ satisfies the master equation for the two-TED system (see Appendix F)

$$\begin{aligned} \dot{\rho} = & -\frac{i}{\hbar}[H, \rho] + \gamma_s \mathcal{L}[w_s] \rho + \gamma_m \mathcal{L}[w_m] \rho \\ & + \sqrt{(1 - \eta^2)\gamma_s\gamma_m} \left(\mathcal{L}_2[w_s, w_m] \rho \right. \\ & \left. + \mathcal{L}_2[w_m, w_s] \rho \right) \end{aligned} \quad (6)$$

where $\mathcal{L}_2[A, B]\rho = A\rho B^\dagger - \frac{1}{2}\{A^\dagger B, \rho\}$ and the Hamiltonian

$$H = H_s + H_m + \frac{i}{2}\sqrt{(1 - \eta^2)\gamma_s\gamma_m} (w_s^\dagger w_m - w_s w_m^\dagger). \quad (7)$$

In Eq. 7, we have neglected terms that describe the phase evolution of the photon in the cabling. We justify this by noting that the detection protocol entangles the mTED's Q_{dm} with photons emitted to the continuum by the mTED's detection protocol. This effectively traces over the photon state space resulting in a mixed state on Q_{dm} . Hence the phase evolution of the itinerant microwave photon is unimportant to describing the demonstration in this paper. See Appendix F for derivations of Eq. (7)–including phase evolution terms–and the collapse operators in Eq. (6).

IV. RESULTS

A. Release and detect demonstration

We configured the sTED and mTED as described in Section III C. Fig. 5a shows a protocol where Q_{ds} and Q_{dm} were excited, preparing $|1010\rangle$. The sTED then releases a photon while the mTED detection is active. The TEDs are connected with a circulator, such that a photon sent from the sTED is received by the mTED. During a detection event the mTED emits photons which are routed to an output measurement line as depicted in Fig. 5b. Using the measured waveguide wavefunction produced by the sTED (section III A) and simulating the Fock state interaction with the mTED (section III C), we predict that $\sim 5\%$ of the sTED's photon wavefunction is clipped by the mTED's bandwidth.

The demonstration in Fig. 5c shows the average population of Q_{dm} as a function of both ϕ_{pm} (tuning ω_{wm}) and the parametric frequency ω_{pm} applied to the DTC's flux line. Together these parameters guarantee an ideal resonant condition (black star) with the incident sTED photon. For the $2\mu\text{s}$ detection window and $4\mu\text{s}$ readout

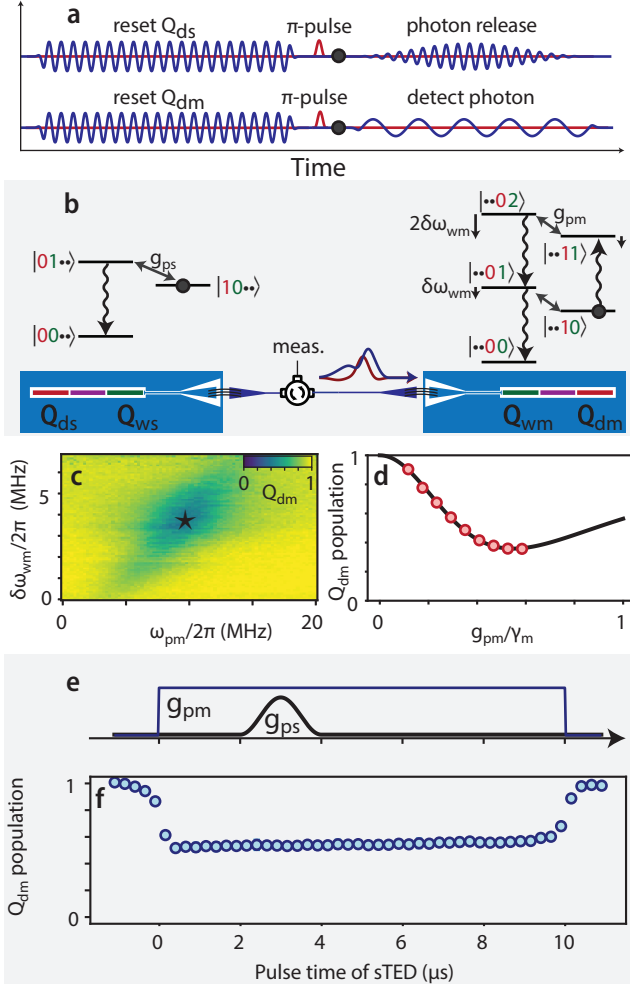


FIG. 5. (a) Protocol of (top) g_{ps} and (bottom) g_{pm} to perform a pitch and detect demonstration. The red traces correspond to operations on (top) Q_{ds} and (bottom) Q_{dm} . (b) (left) Turning on g_{ps} drives an excitation from Q_{ds} into Q_{ws} , which rapidly decays, emitting a photon into the waveguide. A circulator eliminates resonant modes in the cables while also allowing photons to be collected and measured. When the photon arrives at the mTED (right) the population of Q_{dm} goes to zero. (c) Normalized population of Q_{dm} , inverse from the probability of detecting a photon, is plotted as a function of $\delta\omega_{wm}$ and $\delta\omega_{pm}$. $\delta\omega_{wm}$ and $\delta\omega_{pm}$ correspond to excursions from ω_w and $\omega_w - \omega_d - \nu_w$ by varying $\bar{\phi}_p$ and ω_p , respectively. The star indicates where detection probability is maximized. (d) Population of Q_{dm} as a function of g_{pm} measured at the star in panel c. The line is a prediction from the model for which η is a free parameter. The size of the markers is similar to the error. (e) Timing of g_{pm} , corresponding to the detection window (blue), and g_{ps} , where the pulse time (3 μ s in this schematic) denotes the middle of the pulse relative to the beginning of the detection window. (f) Detection fidelity is largely unchanged by the arrival time of the photon. The size of the markers is similar to the error.

used in Fig. 5c-d Q_{dm} has 92 % population-consistent with its T_1 relaxation time—when no photons are detected (8 % dark counts). In Figures 5c-d and f, the population of Q_d is normalized to the scale 0 → 1 corresponding to the probability 1 → 0 of detecting a photon. Figure 5d shows Q_d ’s normalized population as a function of parametric drive amplitude g_{pm} at the ideal resonance condition. Simulations show that at $g_{pm} = \gamma_m/2$ the mTED has a 95 % chance of detecting an incident photon. Thus we infer that 35 % of the sTED’s photons are lost in the setup described in Fig. 5b, which includes approximately a meter of non-superconducting coaxial cable and a circulator.

To highlight the classical behavior of the mTED we show in Fig. 5e-f that the arrival time of the sTED photon within the mTED’s 10 μ s detection window has minimal effect on the detection probability. The slight slope can be attributed to relaxation of the Q_{ds} between its excitation and the release of the photon. The difference in overall maximum detection probability between Fig. 5c-d and Fig. 5f is attributable to reading out after a 10 μ s detection window rather than the 2 μ s. Dark counts also increase to 16 % with the larger detection window.

V. CONCLUSIONS

Inserting a DTC between Q_d and a waveguide provides drop-in photon emission and detection capability without damaging the lifetime and coherence of Q_d . Furthermore, the frequency of Q_d can be independent of Q_w , which is convenient for compatibility with the strict frequency-setting requirements of transmon QPUs. The ~ 300 MHz tuning range of Q_w relaxes frequency setting requirements for networking between dissimilar QPUs. Microwave to optical transducers can have significant variability in their microwave resonant frequencies and hence frequency tunability of Q_w is helpful to interface superconducting QPUs with optical network infrastructure. One additional feature, as highlighted by the transition selectivity of the mTED in detection mode, the TED can be operated as a transition selective photon source. This allows information to be stored in the second excited state of Q_{ds} in an sTED during emission, which is useful for type-II entanglement heralding [48].

The TED can be reconfigured as a sTED or mTED by simply changing the parametric drive, which is a key advantage of this system. This allows the system to be incorporated into different networking protocols without requiring any hardware or setup changes.

ACKNOWLEDGMENTS

DLC, SM, MA, AM, VH, and ML gratefully acknowledge support from AFOSR under LRIR 22RICOR003. We’d like to thank Yuvraj Mohan and the Rigetti Quantum Foundry Services team for design support and de-

vice fabrication. The authors also gratefully acknowledge support from MIT Lincoln Laboratory and IARPA LogiQ program for the traveling wave parametric amplifiers (TWPAs) used in the measurement chains for this work. VH acknowledges support from Hamilton College. Any opinions, findings, and conclusions or recommendations expressed in this article are those of the authors and do not necessarily reflect the views of the Air Force Research Laboratory (AFRL). Approved for Public Release; Distribution Unlimited: PA# AFRL-2026-0214.

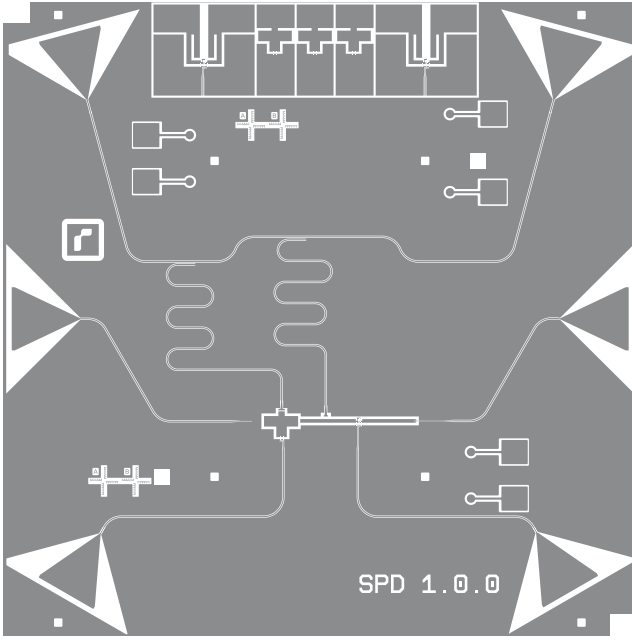


FIG. 6. Full chip layout for the device under test. A cap chip, indium bump bonded to the chip shown, connects the various ground planes.

Appendix A: The TED device

The sTED and mTED devices were fabricated on $6.25 \text{ mm} \times 6.25 \text{ mm}$ high-resistivity silicon chips using Rigetti foundry services. The circuit ground planes are connected via indium bump bonds to a cap chip in a flip-chip configuration. We measured all our flip-bonded chips to have crosstalk less than 1% between flux lines.

The TED device layout is shown in Fig. 6 and parameters are shown in Table I.

The Q_d and Q_w transmon energy levels, calculated with Qutip [49] and verified with Scqubits [50], are shown side-by-side in Fig. 7a. In Fig. 7b we organize the states $|n_d n_w\rangle$ so that each step to the right increments the excitation level of Q_d . Stepping vertically up or down corresponds to the absorption or emission of a photon at Q_w . In this construction, a long-lived state, such as an excited state of Q_d , does not have another state beneath it.

Appendix B: TED Hamiltonian

We define the charge and flux operators on transmon $q \in \{d, c, w\}$ of a single TED (hence we drop index $x \in \{s, m\}$) as \hat{Q}_q and $\varphi_0 \hat{\phi}_q$, respectively, where $\varphi_0 = \Phi_0/2\pi$ and Φ_0 is the magnetic flux quantum. We use hats to help distinguish the charge and flux operators from the transmon and parametric external flux labels in the main text. Junction energies and capacitances have the circuit configuration shown in Fig. 1b. The TED Hamiltonian

Parameter	Value
frequencies	
$\omega_{ds}/2\pi$	3.155 GHz
$\omega_{dm}/2\pi$	2.95 GHz
$\omega_{cx}/2\pi$	3.87(1) GHz
$\omega_{wx}/2\pi$	5.65811(1) GHz
coupling	
$g_{Cx}/2\pi$	~ 0.07 GHz
$g_{Lx}(\Phi_p = 0)/2\pi$	0.30(1) GHz
anharmonicities	
$\nu_{dx}/2\pi$	-0.174(6) GHz
$\nu_{cx}/2\pi$	-0.169(2) GHz
$\nu_{wx}/2\pi$	-0.169(2) GHz
decay rates	
γ_x	$11.2(1) \times 10^6 \text{ s}^{-1}$
drive frequencies	
ω_{ps}	2.5028 GHz
ω_{pm} (reset)	2.541 GHz
ω_{pm} (detection)	2.372 GHz
Junction energies	
E_{Jd}/h	8.7 GHz
E_{Jc}/h	13 GHz
E_{Jw}/h	26 GHz
E_{Jcw}/h	2.2 GHz
capacitances	
C_d	121 fF
C_c	112 fF
C_w	110 fF
C_{dc}	3.8 fF
C_{cw}	~ 7 fF
C_v	4.5 fF
M_d	1 pH
M_p	3 pH

TABLE I. Table of parameters for the mTED and sTED. Indices $x \in \{s, m\}$ distinguish between the sTED and mTED, respectively. M_d and M_p are the mutual inductances of the respective flux lines for Q_{dx} and the DTC of each TED.

then takes the form

$$H = \mathcal{Q}^T \check{C}^{-1} \mathcal{Q} \quad (B1)$$

$$\begin{aligned} & -E_{Jd} \cos(\hat{\phi}_d) - E_{Jc} \cos(\hat{\phi}_c + \phi_{pc}) \\ & - E_{Jw} \cos(\hat{\phi}_w + \phi_{pw}) \\ & - E_{Jcw} \cos(\hat{\phi}_w - \hat{\phi}_c + \phi_{pcw}) \end{aligned} \quad (B2)$$

where

$$\check{C} = \begin{pmatrix} C_d + C_{dc} & -C_{dc} & 0 \\ -C_{dc} & C_c + C_{dc} + C_{cw} & -C_{cw} \\ 0 & -C_{cw} & C_w + C_{cw} + C_v \end{pmatrix} \quad (B3)$$

$$\mathcal{Q}^T = (\hat{Q}_d \ \hat{Q}_c \ \hat{Q}_w) \quad (B4)$$

$$\phi_p = \phi_{pc} + \phi_{pcw} + \phi_{pw} \quad (B5)$$

$$\frac{\phi_{pc}}{\phi_p} = \frac{C_{cw} C_w}{\det(\check{C})}, \quad \frac{\phi_{pcw}}{\phi_p} = \frac{C_c C_w}{\det(\check{C})}, \quad \frac{\phi_{pw}}{\phi_p} = \frac{-C_{cw} C_c}{\det(\check{C})}.$$

Modulating the flux across an inductor also induces a time dependent charge across the capacitor in parallel

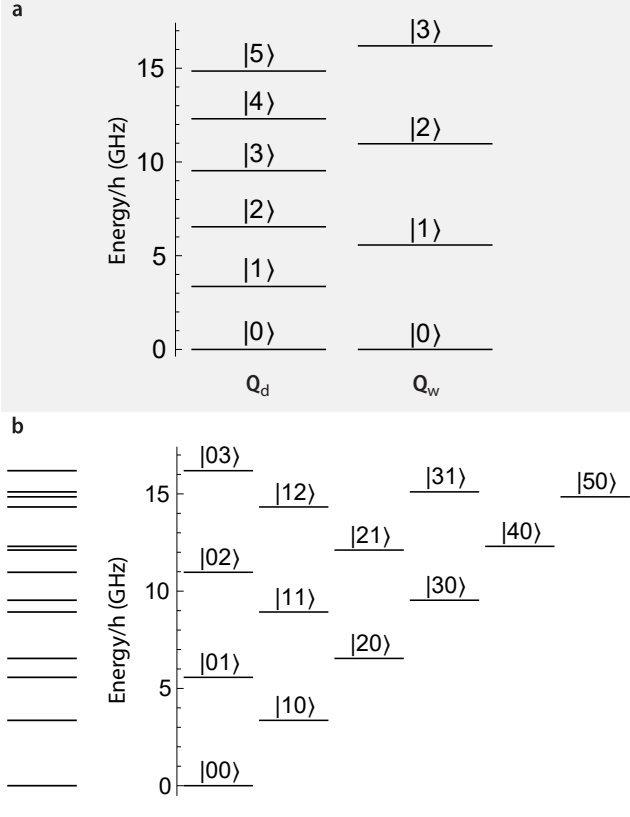


FIG. 7. (a) Energy levels of Q_d and Q_w . (b) Energy levels of a TED, labeled $|n_d n_w\rangle$. Each step to the right increments n_d by one. The levels are overlaid in the left subpanel.

with the inductor [51]. Our choice of the external flux $\{\varphi_0\phi_{pc}, \varphi_0\phi_{pcw}, \varphi_0\phi_{pw}\}$ dropped across each inductive branch cancels these induced charges. Other distributions of branch fluxes in Eq. B1 would yield a correct result if the appropriate time-dependent induced charge terms were included.

1. Harmonic oscillator basis

We convert to the harmonic oscillator basis to isolate terms of interest from Eq. B1. Using index $q \in \{d, c, w\}$ we may make a substitution for the charge and flux operators

$$\hat{Q}_q = \sqrt{\frac{\hbar}{2Z_q}}(a_q + a_q^\dagger) \quad (\text{B6})$$

$$\hat{\phi}_q = \frac{-i}{\varphi_0} \sqrt{\frac{\hbar Z_q}{2}}(a_q - a_q^\dagger) \quad (\text{B7})$$

$$[\varphi_0\hat{\phi}_q, \hat{Q}_q] = i\hbar \quad (\text{B8})$$

where a poor choice of Z_q can still yield accurate numerical results if enough harmonic oscillator levels are included in a simulation. Using the spanning tree

method [52] to obtain \check{C} and \check{L}^{-1} , we choose $Z_q = \sqrt{\check{C}_{q,q}^{-1}/\check{L}_{q,q}^{-1}}$ as the effective qubit impedance where $\check{C}_{q,q}$ and $\check{L}_{q,q}^{-1}$ are diagonal elements of their respective matrices. A procedure for defining an inverse linear inductance for a junction element biased with an external flux is to first substitute $E_{Jk} = \varphi_0^2/L_k$ for $k \in \{c, w, cw\}$ then use the sum trigonometric identity to expand the junction cosine terms

$$-E_{Jk} \cos(\hat{\phi}_k + \phi_{pk}) = -\frac{\varphi_0^2}{L_k} [\cos(\hat{\phi}_k) \cos(\phi_{pk}) - \sin(\hat{\phi}_k) \sin(\phi_{pk})] \quad (\text{B9})$$

$$- \sin(\hat{\phi}_k) \sin(\phi_{pk})] \quad (\text{B10})$$

where $\hat{\phi}_{cw} = \hat{\phi}_w - \hat{\phi}_c$. Then we keep and relabel terms quadratic in $\hat{\phi}_k$:

$$\frac{\hat{\phi}_k^2 \varphi_0^2}{L_k(\phi_{pk})} = \frac{\cos(\phi_{pk}) \hat{\phi}_k^2 \varphi_0^2}{L_k}. \quad (\text{B11})$$

The quadratic term of $E_d \cos(\hat{\phi}_d)$ is simply $\hat{\phi}_d^2 \varphi_0^2 / L_d$. Using this procedure we may collect the coefficients of the identified terms to construct an effective inverse inductance matrix from Eq. B1

$$\check{L}^{-1} = \begin{pmatrix} \frac{1}{L_d} & 0 & 0 \\ 0 & \frac{1}{L_c(\phi_{pc})} + \frac{1}{L_{cw}(\phi_{pcw})} & -\frac{1}{L_{cw}(\phi_{pcw})} \\ 0 & -\frac{1}{L_{cw}(\phi_{pcw})} & \frac{1}{L_w(\phi_{pw})} + \frac{1}{L_w(\phi_{pcw})} \end{pmatrix}. \quad (\text{B12})$$

A rough estimate of the coupling—typically accurate to within 30%—can be obtained by substituting the harmonic oscillator transformation into the inductive coupling branch of the DTC and taking $\phi_{pcw} \rightarrow \phi_p$ and $\phi_{pc}, \phi_{pw} \rightarrow 0$. The closure branch junction term may be expanded using trigonometric identities

$$\begin{aligned} & \cos(\hat{\phi}_w - \hat{\phi}_c + \phi_p) = \\ & [\cos(\hat{\phi}_w) \cos(\hat{\phi}_c) + \sin(\hat{\phi}_w) \sin(\hat{\phi}_c)] \cos(\phi_p) \\ & - [\sin(\hat{\phi}_w) \cos(\hat{\phi}_c) - \cos(\hat{\phi}_w) \sin(\hat{\phi}_c)] \sin(\phi_p), \end{aligned} \quad (\text{B13})$$

then we may collect terms proportional to $\hat{\phi}_w \hat{\phi}_c$

$$-E_{Jcw} \hat{\phi}_w \hat{\phi}_c \cos(\phi_p), \quad (\text{B14})$$

and finally apply the harmonic oscillator basis transformation

$$\frac{\hbar \sqrt{Z_w Z_c}}{2L_{Jcw}} \cos(\phi_p) (a_w - a_w^\dagger) (a_c - a_c^\dagger) \quad (\text{B15})$$

$$\approx \hbar g_L(\phi_p) (a_w - a_w^\dagger) (a_c - a_c^\dagger). \quad (\text{B16})$$

Note that the $\sin(\phi_w) \cos(\phi_c) - \cos(\phi_w) \sin(\phi_c)$ terms thrown away in Eq. B14 would make a lesser, but still substantial, correction to the entangling interaction in Eq. B15.

Experimentally, we sinusoidally modulate $\phi_p = \bar{\phi}_p + A_\phi(t) \sin(\omega t)$, where $A_\phi(t)$ is a dimensionless amplitude

and $\bar{\phi}_p$ is the time averaged dimensionless flux. In the limit where $A_\phi(t) \ll 2\pi$

$$\begin{aligned}\cos(\phi_p) &= \cos(\bar{\phi}_p + A_\phi(t) \sin(\omega_p t)) \\ &= \cos(\bar{\phi}_p) \cos(A_\phi(t) \sin(\omega_p t)) \\ &\quad - \sin(\bar{\phi}_p) \sin(A_\phi(t) \sin(\omega_p t)) \\ &\approx \cos(\bar{\phi}_p) - A_\phi(t) \sin(\bar{\phi}_p) \sin(\omega_p t)\end{aligned}\quad (\text{B17})$$

From this expansion, we can estimate the time-independent and time-dependent parts of $g_L(t) = \bar{g}_L + A(t) \sin(\omega_p t)$

$$\bar{g}_L \approx \frac{\hbar\sqrt{Z_w Z_c}}{2L_{cw}} \cos(\bar{\phi}_p) \quad (\text{B18})$$

$$A(t) \approx -\frac{\hbar\sqrt{Z_w Z_c}}{2L_{cw}} A_\phi(t) \sin(\bar{\phi}_p) \quad (\text{B19})$$

Appendix C: Effective TED Hamiltonian derivation

Modeling the behavior of a TED can be computationally intensive since Q_d , Q_c , and Q_w should have very different frequencies and there is at least one high-frequency driving term. In this section we will derive the effective stationary Hamiltonian used in the text, starting with a harmonic oscillator approximation of the exact Hamiltonian in Eq. B1.

$$\begin{aligned}\frac{H}{\hbar} &= \sum_{q=\{d,c,w\}} [\omega_q q^\dagger q + \nu_q q^{\dagger 2} q^2] \\ &\quad + g_C(d + d^\dagger)(c + c^\dagger) \\ &\quad - g_L(t)(c - c^\dagger)(w - w^\dagger) \\ &\quad - i\Omega(t) \sin(\omega_\alpha t)(w - w^\dagger).\end{aligned}\quad (\text{C1})$$

To make the parametric drive stationary, we impose a rotating frame transformation $d \rightarrow de^{-i\omega_p t}$ and $c \rightarrow ce^{-i\omega_p t}$, resulting in the Hamiltonian

$$\begin{aligned}\frac{H}{\hbar} &= \left[(\omega_d + \omega_p)d^\dagger d + (\omega_c + \omega_p)c^\dagger c + \omega_w w^\dagger w \right. \\ &\quad + \sum_{q=\{d,c,w\}} \nu_q q^{\dagger 2} q^2 \\ &\quad + g_C(cde^{2i\omega_p t} + cd^\dagger + c^\dagger d + c^\dagger d^\dagger e^{-2i\omega_p t}) \\ &\quad - (B + A(t) \sin(\omega_p t))(ce^{i\omega_p t} - c^\dagger e^{-i\omega_p t})(w - w^\dagger) \\ &\quad \left. - i\Omega(t) \sin(\omega_\alpha t)(w - w^\dagger) \right].\end{aligned}\quad (\text{C2})$$

We then apply the rotating wave approximation to eliminate fast rotating terms proportional to $e^{2i\omega_p t}$, resulting

in the new Hamiltonian

$$\begin{aligned}\frac{H}{\hbar} &= \left[(\omega_d + \omega_p)d^\dagger d + (\omega_c + \omega_p)c^\dagger c + \omega_w w^\dagger w \right. \\ &\quad + \sum_{q=\{d,c,w\}} \nu_q q^{\dagger 2} q^2 \\ &\quad + g_C(cd^\dagger + c^\dagger d) + A(t)(c^\dagger w - cw^\dagger)/2i \\ &\quad \left. - i\Omega(t) \sin(\omega_\alpha t)(w - w^\dagger) \right].\end{aligned}\quad (\text{C3})$$

Similarly, if there is a coherent drive we may perform the simultaneous transformations $d \rightarrow de^{-i\omega_\alpha t}$, $c \rightarrow ce^{-i\omega_\alpha t}$, and $w \rightarrow we^{-i\omega_\alpha t}$ to obtain

$$\begin{aligned}\frac{H}{\hbar} &= \left[(\omega_d + \omega_p - \omega_\alpha)d^\dagger d + (\omega_c + \omega_p - \omega_\alpha)c^\dagger c \right. \\ &\quad + (\omega_w - \omega_\alpha)w^\dagger w + \sum_{q=\{d,c,w\}} \nu_q q^{\dagger 2} q^2 \\ &\quad + g_C(cd^\dagger + c^\dagger d) \\ &\quad \left. + A(t)(c^\dagger w - cw^\dagger)/2i + \Omega(t)(w + w^\dagger)/2 \right].\end{aligned}\quad (\text{C4})$$

In the next section we will eliminate the Q_c mode to recover the equation in the main text.

1. Adiabatic elimination of Q_c

The coupling qubit Q_c mediates a virtual interaction between Q_d and Q_w . This effective interaction may be computed using the Schrieffer-Wolff transformation

$$H' = e^S H e^{-S} \quad (\text{C5})$$

$$S = \frac{g_C}{\omega_d - \omega_c}(d^\dagger c - c^\dagger d) + \frac{-A(t)/2i}{\omega_w - (\omega_c + \omega_p)}(w^\dagger c + c^\dagger w) \quad (\text{C6})$$

The Schrieffer-Wolff procedure is to divide a Hamiltonian into on-site and coupling terms: $H \approx H_0 + V$. Starting from Eq. (C3) while neglecting the anharmonicity and coherent drive terms

$$H_0 = (\omega_d + \omega_p)d^\dagger d + (\omega_c + \omega_p)c^\dagger c + \omega_w w^\dagger w \quad (\text{C7})$$

$$V = g_C(cd^\dagger + c^\dagger d) + A(t)(c^\dagger w - cw^\dagger)/2i \quad (\text{C8})$$

$$H' = H_0 + V + [S, H_0] + \frac{1}{2}[S, V] + \mathcal{O}(V^3). \quad (\text{C9})$$

S was chosen so that $V + [S, H_0] = 0$, leaving $\frac{1}{2}[S, V]$ as the lowest-order interaction term. Plugging in for S and V we obtain

$$\begin{aligned}\frac{1}{2}[S, V] &= \left[\frac{-g_C A(t)}{4i(\omega_d - \omega_c)} + \frac{-g_C A(t)}{4i(\omega_w - (\omega_c + \omega_p))} \right] \\ &\quad \times (w^\dagger d - wd^\dagger) \\ &\quad + \frac{-g_C^2}{(\omega_d - \omega_c)}(d^\dagger d - c^\dagger c) \\ &\quad + \frac{-A^2(t)}{4(\omega_w - (\omega_c + \omega_p))}(w^\dagger w - c^\dagger c)\end{aligned}\quad (\text{C10})$$

where the term proportional to $w^\dagger d - wd^\dagger$ is an effective interaction term mediated by a driving field. The terms proportional to $d^\dagger d$, $c^\dagger c$, and $w^\dagger w$ are corrections to the frequencies ω_d , ω_c , and ω_w , respectively. In the resonant case $\omega_p = \omega_w - \omega_d$, the effective coupling simplifies to

$$H_{\text{int}} = -ig_p(t)(d^\dagger w - dw^\dagger) \quad (\text{C11})$$

$$g_p(t) = \frac{g_C A(t)}{2(\omega_d - \omega_c)} \quad (\text{C12})$$

Transforming into the rotating frame of an external coherent drive—as done between Eq. (C3) and Eq. (C4)—then adding back in the anharmonicity terms, we recover the equation used in the main text:

$$H/\hbar = \left[(\delta - \delta_p)d^\dagger d + \delta w^\dagger w + \nu_d d^{\dagger 2} d^2 + \nu_w w^{\dagger 2} w^2 - ig_p(t)(d^\dagger w - dw^\dagger) + \Omega(t)(w + w^\dagger)/2 \right] \quad (\text{C13})$$

$$\delta_p = \omega_w - \omega_d \pm \omega_p \quad (\text{C14})$$

$$\delta = \omega_w - \omega_\alpha. \quad (\text{C15})$$

The sign choice in Eq. C14 should minimize the magnitude of δ_p .

Appendix D: Optimizing for Q_d coherence and ease of operation

Shifting of the frequency of Q_w as a function of drive amplitude $A(t)$ complicates waveguide photon shaping and capture. While these distortions can be measured and corrected with the arbitrary waveform generator (AWG) on the DTC’s flux drive line it is often better to passively mitigate the shift.

In the main text we identify two origins to the frequency shift with $A(t)$. The first is an ac Stark shift $A(t)^2/4(\omega_d - \omega_c)$ of ω_w and the second is rectification from curvature in the dispersion of $\omega_w(\phi_p)$. The maximum desired value for $A(t)$ is given by $g_p = g_C A/2(\omega_d - \omega_c) = \gamma/2$. Distortion of the outgoing photon wavefunction increases with the *ratio* of the ac Stark shift of ω_w over g_p and so $A \leq g_C/2$. For high coherence Q_d it is useful to keep the coupling between Q_d and Q_c in the dispersive limit: $g_C \leq 0.1|\omega_d - \omega_c|$.

Taking the upper limit of the two inequalities in the paragraph above: we substitute $g_C = 0.1|\omega_d - \omega_c|$ and $A = g_C/2 = 0.1|\omega_d - \omega_c|/2$ into $g_C A/2(\omega_d - \omega_c) = \gamma/2$. We can write the optimization condition in terms of the detuning

$$0.005|\omega_d - \omega_c| \gg \gamma. \quad (\text{D1})$$

The above approach also reduces rectification by reducing the required amplitude of A . We can further reduce rectification by increasing the slope of $\omega_w(\phi_p)$ so we may modulate ϕ_p with a smaller amplitude to obtain the same $A(t)$. While increasing the value of E_{Jcw} accomplishes this it also increases many noise terms. We cap the value $E_{Jcw} \leq 0.2 \min(E_{Jc}, E_{Jw})$.

Appendix E: Calculating relaxation of the data qubit

Referring to the circuit in Fig. 1b, we use a perturbative approach for calculating an equivalent $1/RC$ decay rate for Q_d . This approach uses the admittance of the node associated with Q_d to ground where the waveguide is replaced with a 50Ω resistor to ground

$$A \parallel B = \frac{1}{\frac{1}{A} + \frac{1}{B}} \quad (\text{E1})$$

$$Y(\omega) = i\omega C_d + \frac{1}{i\omega L_d} + i\omega C_{dc} \parallel \left(i\omega C_c + \frac{1}{i\omega L_c} + i\omega C_{dw} \parallel \left(i\omega C_w + \frac{1}{i\omega L_w} + i\omega C_v \parallel \frac{1}{50\Omega} \right) \right) \quad (\text{E2})$$

$$\Gamma \approx \frac{\text{Re}(Y(\omega_d))}{C_d + C_{dc}}. \quad (\text{E3})$$

This approach is valid when the node of interest is only weakly hybridized with other nodes of the circuit.

Appendix F: Release and Detect Simulations

The release-and-detect experiment consists of three localized components (two TEDs and a circulator, Fig. 8a) networked together via itinerant bosonic modes. This network of devices is well-suited to a mathematical description via the SLH framework [45–47]

In the SLH framework, localized components are described in terms of the triple (S, L, H) of scattering matrix, vector of Lindblad operators, and Hamiltonian. From this local description and the network topology, the SLH triple for the full network can be derived via three types of operation. The cascade operation between components C_1 and C_2 , represented as $C_2 \triangleleft C_1$, sends the output from each port of component 1 into the corresponding input port of component 2. The concatenate operation between a P_1 -port component and a P_2 -port component, represented as $C_1 \boxplus C_2$, combines the two components into a single $(P_1 + P_2)$ -port component. The feedback operation on a component C , represented as $[C]_{x \rightarrow y}$, feeds the output of port x into input port y of the same component. The master equation for a component with P ports and SLH triple (S, L, H) is then given by

$$\dot{\rho} = -\frac{i}{\hbar}[H, \rho] + \sum_{p=1}^P \mathcal{L}[L_p]\rho. \quad (\text{F1})$$

A TED is a two-port component whose first port couples to right-moving modes and whose second port couples to left-moving modes. Its Hamiltonian H_{TED} is given by Equation (4), and its SLH triple is

$$\text{TED} = \left(\begin{bmatrix} 1 & 0 \\ 0 & 1 \end{bmatrix}, \begin{bmatrix} \sqrt{\frac{\gamma}{2}}w \\ \sqrt{\frac{\gamma}{2}}w \end{bmatrix}, H_{\text{TED}} \right). \quad (\text{F2})$$

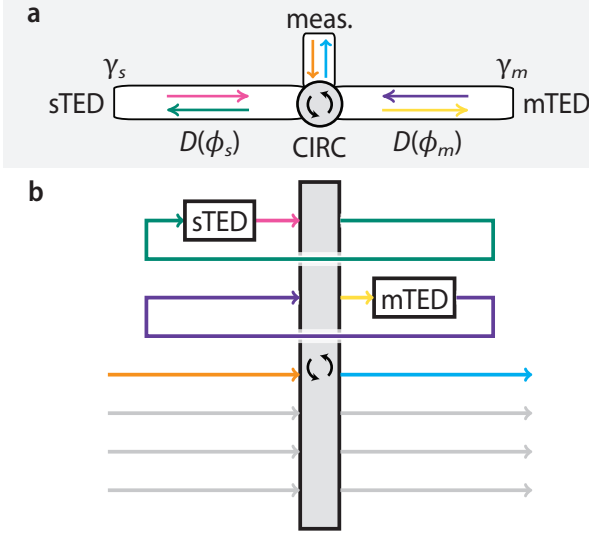


FIG. 8. (a) The sTED emits a signal, which gains a phase ϕ_s while traveling a waveguide to a circulator (CIRC) and gains a phase ϕ_m traveling to mTED, where it is detected. (b) The SLH diagram for this system includes three fictitious ports (grey arrows) introduced to model circulator loss. The other signal path arrows are color-coded to emphasize the connection between (a) and (b).

In our release-and-detect experiment, the source (sTED) and detector (mTED) both terminate the waveguide and thus are one-port components (as shown in Fig. 8b). The termination is modeled in the SLH framework via a feedback operation, and thus the x TED for $x \in \{s, m\}$ has SLH triple

$$[\text{TED}]_{1 \rightarrow 2} = [\text{TED}]_{2 \rightarrow 1} = \left(1, \sqrt{2\gamma_x} w_x, H_x \right). \quad (\text{F3})$$

The waveguide termination modifies the density of states in the waveguide, enhancing the coupling between the TED and the waveguide. This enhancement appears as a factor of 2 in Equation (F3), which we absorb into the definition of the decay rate γ_x (this is now the experimental decay rate) to define the one-port x TED components as

$$\text{TED}_{\text{one-port}} = (1, \sqrt{\gamma_x} w_x, H_x). \quad (\text{F4})$$

A lossy three-port circulator that directs inputs at port p to output $p+1$ is represented by the SLH triple

$$\text{CIRC} = \left(\begin{bmatrix} 0 & 0 & \bar{\eta} & -\eta & 0 & 0 \\ \bar{\eta} & 0 & 0 & 0 & -\eta & 0 \\ 0 & \bar{\eta} & 0 & 0 & 0 & -\eta \\ 0 & 0 & \eta & \bar{\eta} & 0 & 0 \\ \eta & 0 & 0 & 0 & \bar{\eta} & 0 \\ 0 & \eta & 0 & 0 & 0 & \bar{\eta} \end{bmatrix}, \begin{bmatrix} 0 \\ 0 \\ 0 \\ 0 \\ 0 \\ 0 \end{bmatrix}, 0 \right), \quad (\text{F5})$$

where $\eta \in [0, 1]$ is a loss parameter, $\bar{\eta} = \sqrt{1 - \eta^2}$, and the last three ports represent loss channels (see Fig. 8b).

The components are networked together via approximately one meter of coaxial cable. The timescale for signal propagation between components, $\text{distance}/v \sim \mathcal{O}(\text{ns})$, is significantly shorter than the timescale of the system dynamics, $2\pi/\gamma \sim \mathcal{O}(\mu\text{s})$. In this regime, and under the assumption that the cable is dispersionless and linear, it is appropriate to model signal propagation through the cable as a phase delay component $D(\phi) = (e^{i\phi}, 0, 0)$. We take the phase due to propagation between the sTED and circulator to be ϕ_s and the delay due to propagation between the circulator and mTED to be ϕ_m .

The full network for the release-and-detect experiment is then described by the SLH expression (where I_n is an n -port identity component)

$$\begin{aligned} & \left[(I_1 \boxplus \text{mTED} \boxplus I_4) \triangleleft (D(\phi_s) \boxplus D(\phi_m) \boxplus I_4) \right. \\ & \triangleleft \text{CIRC} \triangleleft (D(\phi_s) \boxplus D(\phi_m) \boxplus I_4) \\ & \left. \triangleleft (\text{sTED} \boxplus I_5) \right]_{1 \rightarrow 1, 2 \rightarrow 2}. \end{aligned} \quad (\text{F6})$$

The overall model can be interpreted as a sequence of cascaded modules corresponding to the signal path shown in Fig. 8a. In this expression, the first port corresponds to the waveguide connecting the sTED to the circulator, the second port corresponds to the coaxial cable connecting the circulator to the mTED, the third port corresponds to the measurement port of the circulator, and the remaining three ports are loss ports. In this formalism, the series cascade operator (\triangleleft) connects modules sequentially—with the signal path propagating from right to left—while the concatenation operator (\boxplus) arranges components in parallel. Thus, reading Eq. (F6) from right to left, the sTED emits a signal into port 1, where it travels through the waveguide and picks up a phase of ϕ_s before entering the circulator. The circulator redirects the signal (minus some loss) to port 2, where it propagates through the coaxial cable and picks up a phase of ϕ_m before entering the mTED. Due to the feedback operation, the output of the mTED is directed back into port 2 (at the right side of the expression), where it propagates through the coaxial cable and picks up a phase of ϕ_m before entering the circulator. The circulator redirects the signal (minus some loss) to port 3, from which the signal leaves the system.

This results in the master equation

$$\begin{aligned} \dot{\rho} = & -\frac{i}{\hbar} [H, \rho] + \gamma_s \mathcal{L}[w_s] \rho + \gamma_m \mathcal{L}[w_m] \rho \\ & + \sqrt{(1 - \eta^2) \gamma_s \gamma_m} \left(\mathcal{L}_2[w_s, e^{-i(\phi_s + \phi_m)} w_m] \rho \right. \\ & \left. + \mathcal{L}_2[e^{-i(\phi_s + \phi_m)} w_m, w_s] \rho \right), \end{aligned} \quad (\text{F7})$$

where we define $\mathcal{L}_2[A, B]\rho = A\rho B^\dagger - \frac{1}{2}\{A^\dagger B, \rho\}$ and the Hamiltonian is given by

$$\begin{aligned} H = & H_s + H_m + \frac{1}{2} \sqrt{(1 - \eta^2) \gamma_s \gamma_m} \\ & \times \left(i e^{-i(\phi_s + \phi_m)} w_s^\dagger w_m - i e^{i(\phi_s + \phi_m)} w_s w_m^\dagger \right). \end{aligned} \quad (\text{F8})$$

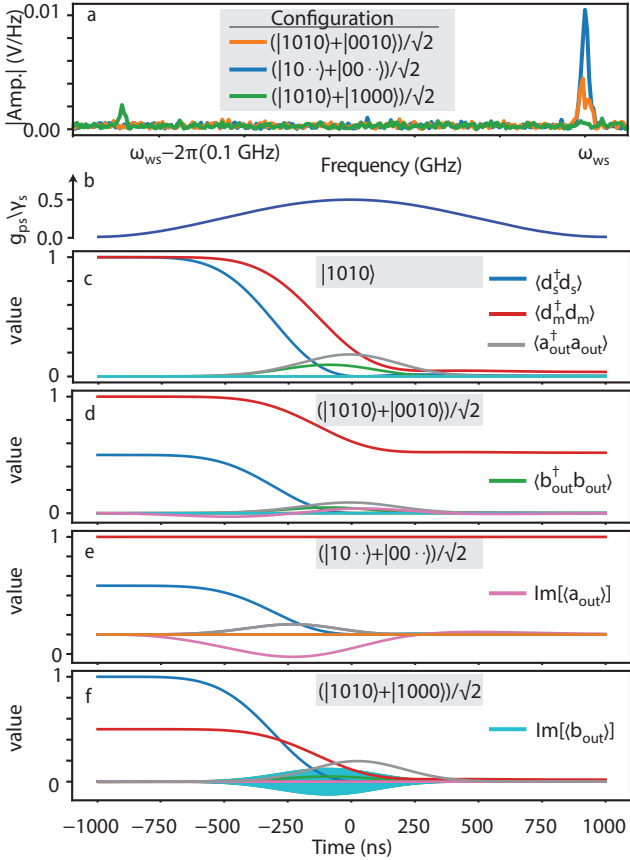


FIG. 9. (a) The signal output along the waveguide is demodulated, measured by a digitizer, and digitally Fast Fourier transformed (FFT) for three initial states $|n_{ds}n_{ws}n_{dm}n_{dw}\rangle$ of the pitch-detect experiment. In (b-f) we show theory for the state evolution of the pitch-detect demonstration while neglecting loss in the waveguide. $|\langle a_{\text{out}} \rangle|$ and $|\langle b_{\text{out}} \rangle|$ are proportional to the experimental data in panel (a) observed at $\omega_{ws}/2\pi$ and $\omega_{ws}/2\pi - 0.108(1) \text{ GHz}$, respectively. The simulation is in a frame that rotates at rate ω_{ws} . (b) Shows the cosine envelope of g_{ps} , which releases the state stored in Q_{ds} . (c) Fock state emission and detection matching the pitch-detect demonstration in the main text. (d) Same as panel (c) where Q_{ds} is instead prepared on the equator of its Bloch sphere. (e) Same as panel (d) where we tune Q_{wm} away from Q_{ws} . (f) Same as panel (c) where we instead prepare Q_{dm} on the equator of its Bloch sphere.

For any output solely generated by the source qubit, the input-output relation [40, 41, 53] has the following form

$$\langle a_{\text{out}} \rangle = e^{i(\phi_s + \phi_m)} \sqrt{\frac{\gamma_s}{2}} \langle w_s \rangle + \sqrt{\frac{\gamma_m}{2}} \langle w_m \rangle \quad (\text{F9})$$

$$\langle w_s \rangle = \text{Tr}[\rho w_s] \quad (\text{F10})$$

$$\langle w_m \rangle = \text{Tr}[\rho w_m]. \quad (\text{F11})$$

Appendix G: Averaged measurements of the waveguide

We put the waveguide emission seen in the measurement chain in context with theoretical quantum state populations of the joint sTED and mTED system. The state populations are structured as described in the main text $|n_{ds}n_{ws}n_{dm}n_{wm}\rangle$, where n denotes the excitation level of each indexed transmon.

The amplitude and phase of a coherent state in a waveguide is given by the expectation value of the lowering operator $\langle a_{\text{out}} \rangle$. This value is proportional to the information retained after averaging a signal many times on a digitizer. We define our waveguide state using Appendix F as $a_{\text{out}} = e^{i(\phi_s + \phi_m)} \sqrt{\gamma_s/2} w_s + \sqrt{\gamma_m/2} w_m^{(01)}$ and $b_{\text{out}} = \sqrt{\gamma_m/2} w_m^{(12)}$ where $w_m^{(01)}$ is the part of the lowering operator w_m that acts on the $0 \leftrightarrow 1$ transition while $w_m^{(12)}$ acts on the $1 \leftrightarrow 2$ transition. Figure 9a shows the fast Fourier transformation (FFT) of digitizer traces averaging over ten thousand measurements. It shows peaks proportional to $\langle a_{\text{out}} \rangle$ and $\langle b_{\text{out}} \rangle$ for different configurations of the pitch-detect demonstration.

We compare these experimental results to the model in Appendix F using modulation of the envelope of g_{ps} shown in Fig. 9b at frequency $\omega_{ps} = \omega_{ws} - \omega_{ds}$. The mTED is in a detection configuration such that the drive amplitude is $|g_{pm}| = \gamma_m/2$ and its frequency is $\omega_{pm} = \omega_{wm} - \omega_{dm} + \nu_{wm}$. The expectation values $\langle d_s^\dagger d_s \rangle$ and $\langle d_m^\dagger d_m \rangle$ track the populations of the data qubits Q_{ds} and Q_{dm} , respectively. $\langle a_{\text{out}}^\dagger a_{\text{out}} \rangle$ and $\langle b_{\text{out}}^\dagger b_{\text{out}} \rangle$ are proportional to the itinerant microwave photon wavefunction power at the $0 \leftrightarrow 1$ and $1 \leftrightarrow 2$ transition frequencies, respectively. The real part of $\langle a_{\text{out}} \rangle$ is 0 for all times. We do not show $\text{Re}[\langle b_{\text{out}} \rangle]$ because its carrier is simply $\pi/2$ out of phase with $\text{Im}[\langle b_{\text{out}} \rangle]$.

The configuration $|1010\rangle$, corresponding to the main text, shows a Fock state emitted from the sTED that then de-excites the mTED. Note that Q_{dm} does not go all the way to zero. Emission from the $1 \leftrightarrow 2$ transition slightly leads emission from the $0 \leftrightarrow 1$ transition. Preparing Q_{ds} in a superposition means $\langle a_{\text{out}} \rangle$ can be non-zero as shown in Fig. 9d-e (pink curve). The amplitude of $\langle a_{\text{out}} \rangle$ is much smaller in Fig. 9d than Fig. 9e because the mTED is measuring the waveguide state, projecting the waveguide state into a vacuum or Fock state. In Figure 9e we detune ω_{wm} from ω_{ws} so that the sTED's waveguide state is no longer measured. If instead we prepare Q_{dm} in a superposition state, $\langle b_{\text{out}} \rangle$ is non-zero (Fig. 9f, cyan curve). Figure 9f is in the rotating frame of ω_{ws} causing $\langle b_{\text{out}} \rangle$ to have a carrier frequency $\nu_{wm}/2\pi$. Note that ν_{wm} differs from the value listed in Table I because the experiment was reproduced in another cryostat (so we could add the waveguide measurement chain) and a two level system (TLS) avoided level crossing of 84.5(1) MHz appeared 32(1) MHz above $\omega_{wm}/2\pi = 5.7177(2) \text{ GHz}$. The TLS was not present in subsequent cryostat cooldowns.

We further checked the Fock state emission by setting

Q_{ds}	Q_{dm}	$0 \leftrightarrow 1$ (arb.)	$1 \leftrightarrow 2$ (arb.)
0	0	reference	reference
1	0	1.1(2)	0.1(2)
0	1	-0.2(2)	-0.1(2)
1	1	2.1(2)	1.5(2)

TABLE II. For each Q_{ds} and Q_{dm} , ten million measurements were integrated, squared, then averaged. The average for $|0000\rangle$ was subtracted from the other configurations.

Q_{ds} and Q_{dm} to either $|0\rangle$ or $|1\rangle$. We integrated over a single measurement of a_{out} and b_{out} after amplification, squared each, then averaged ten million of these measurements, the result of which is related [40] to $\langle a_{out}^\dagger a_{out} \rangle$ and $\langle b_{out}^\dagger b_{out} \rangle$. These averages are then compiled in Table II where the result for the initial state $|0000\rangle$ was subtracted from the other configurations. We observe photons only if Q_{ds} is initially excited. The last row of the table corresponds to the simulation in Fig. 9c where both Q_{ds} and Q_{dm} are initially excited, a photon is detected, and after amplification signatures of photons at both ω_{ws} and $\omega_{ws} - \nu_{wm}$ are observed.

Appendix H: Coherent scattering off Q_w

Master equations are a convenient tool for modeling near resonance coherent scattering with a qubit [53]. We use this tool to perform the simulation in Fig. 4g. Including thermal terms, the master equation is

$$\dot{\rho} = -\frac{i}{\hbar}[H, \rho] + \gamma(1 + n_{th})\mathcal{L}[w] + \gamma n_{th}\mathcal{L}[w^\dagger] \quad (H1)$$

where n_{th} is the Bose-Einstein mode occupation at a given temperature and frequency.

We define here an RWA Hamiltonian that only includes the waveguide qubit and an external coherent drive term. Using the Hamiltonian Eq. (C13) instead can reveal how the scattering changes as a function of parametric drive power and frequency.

$$H/\hbar = \delta w^\dagger w + \nu_w w^\dagger w^2 + i\Omega(w - w^\dagger)/2 \quad (H2)$$

$$\Omega = 2\sqrt{\frac{2P_\alpha\gamma\omega_\alpha}{\omega_w}} \quad (H3)$$

$$P_\alpha = \gamma\bar{n} \quad (H4)$$

where P_α is the power of the coherent drive and \bar{n} is the average number of coherent photons at frequency ω_α and integrated over time $1/\gamma$. The output state of the waveguide can be written in terms of the input state with the following relation

$$a_{out} = a_{in} + \sqrt{\frac{\gamma}{2}}w \quad (H5)$$

where a_{in} and a_{out} are the lowering operators (with units of $\sqrt{\text{Hz}}$) for waveguide modes that travel towards the

qubit and away from the qubit, respectively. This input-output relation can be used to simulate various moments of the waveguide [11, 16, 40, 41, 54] including coherent and Fock state statistics. For a simulation of coherent scattering the simulation of interest is

$$\langle a_{out} \rangle = \sqrt{\gamma\bar{n}} + \sqrt{\frac{\gamma}{2}}\langle w \rangle \quad (H6)$$

$$\langle w \rangle = \text{Tr}[\rho w]. \quad (H7)$$

The equivalent experimental measurement can be performed with a two-port vector network analyzer.

Appendix I: Cryostat measurement setup

The cryostat measurement setup is shown in Fig. 10 and components are listed in Table III. Pulses were generated using Keysight M3202A arbitrary waveform generators (AWGs) inside of a Keysight M9019A chassis (not pictured), then routed to Rohde & Schwarz (R&S) SGS100A microwave frequency generators. Voltage sources (Yokogawa GS200) were either used in isolation on Q_d flux lines, or coupled via room temperature bias tees (Mini-Circuits ZFBT-6GW+) to R&S RF generators to parametrically drive while still allowing for modification of applied voltage bias. Q_d flux lines were filtered by low pass filters (Mini-Circuits VLFX-300+) to prevent Purcell decay. Readout microwave drives were split into a drive/readout side using a power splitter (Marki Microwave PD0R618) to downconvert (Marki Microwave MMIQ0218LXPC) the received drive signal into the digitization band of the Keysight M3012A. Before digitization, the I/Q signal was amplified with a low-noise amplifier (SRS SR445A). Within the fridge, Radiall switches were used to switch between the different sample feed lines. The cryostat contained two sets of switches. The drive side switches' center pin was used to send signals into the designated connection through 70 dB total attenuation in addition to a 12.5 GHz low-pass filter (RLC F-30-12.4-R). Measurement-side switches' center pins were attached to amplified lines consisting of a travelling-wave parametric amplifier (TWPA) at the mixing chamber (MXC), cryogenic high electron-mobility transistor (HEMT) at the 3K stage, and a room-temperature HEMT above the fridge. Dual-junction circulators were used between the sample and the TWPA to isolate from TWPA back-action, and between the TWPA and cryo-HEMT with similar reasoning. A directional coupler (Marki Microwave C10-0116) is used to couple the TWPA drive pump with the signal line. The circulator (LNF-CICIC4-12A) between the two samples was connected to a measurement-side Radiall switch distinct from the measurement line used for Q_d readout. This allowed readout to be conducted in parallel with waveguide backscatter measurements.

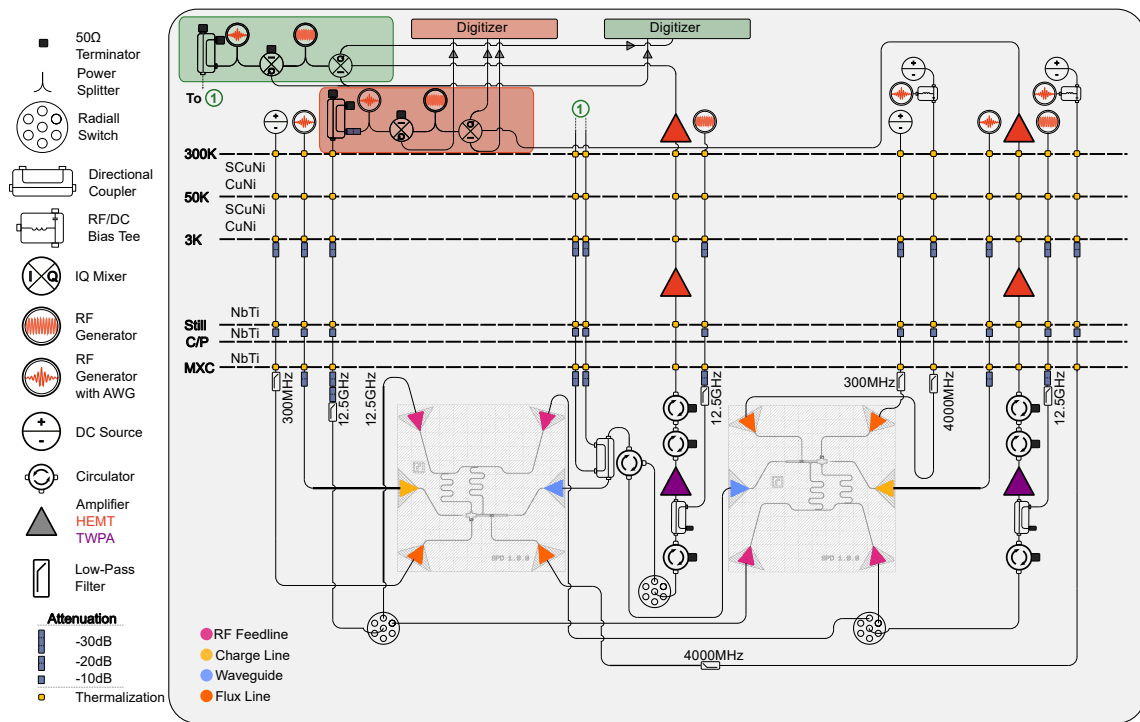


FIG. 10. Diagrammatic representation of the room temperature and cryogenic components used in the described experiments. The readout / digitization circuits are highlighted according to their use: readout used in backscatter measurements to verify waveguide drive power as in Fig. 4f is highlighted in green, and the heterodyne readout circuit used to read out qubits via the readout resonators is highlighted in red.

TABLE III. Components in the Measurement Setup

Component	Manufacturer & Model	Function
PXIe Chassis	Keysight M9019A	Hosts AWG and Digitizer modules
Arbitrary Wave Generator (AWG)	Keysight M3202A	Pulse sequence generation
RF generator	Rohde & Schwarz SGS100A	Upconversion of AWG pulses to RF frequencies
DC Source	Yokogawa GS200	Static flux biasing for transmons
Bias Tee	Mini-Circuits ZFBT-6GW+	Combines RF drive and DC flux bias on a single line
Power Splitter	Marki Microwave PD0R618	Splits readout tone for I/Q downmixing reference
I/Q Mixer	Marki Microwave MMIQ0218LXPC	Downconverts readout signal to baseband
Room Temperature Preamplifier	SRS SR445A 350 MHz	Room temperature pre-amplification before digitization
Digitizer	Keysight M3012A PXIe with FPGA	I/Q signal acquisition and digitization
RF Switch	Radiall R591762600	Switches signal paths between different samples inside the fridge
12.5 GHz Low-Pass Filter	RLC F-30-12.4-R	Filters low-frequency signal lines
300 MHz Low-Pass Filter	Mini-Circuits VLFX-300+	Thermal noise filtering for DC flux lines
10dB Broadband Directional Coupler	Marki Microwave C10-0116	Injects TWPA pump tone into the signal line
Circulator/Isolator	Low Noise Factory LNF-CICIC4-12A	Isolates sample from amplifier back-action and routes signal
Traveling-Wave Parametric Amplifier (TWPA)	MIT Lincoln Laboratory & IARPA LogiQ program	MXC stage, quantum-limited signal amplification
Room temperature High Electron-Mobility Transistor (HEMT)	LNF-LNR4_8C_SV	Readout line room-temperature amplifier
Cryogenic HEMT	Low Noise Factory LNF-LNC4_8	4K stage cryogenic amplifier

[1] J. I. Cirac, A. K. Ekert, S. F. Huelga, and C. Macchiavello, Phys. Rev. A **59**, 4249 (1999).

[2] H. J. Kimble, Nature **453**, 1023 (2008).

[3] C. Monroe, R. Raussendorf, A. Ruthven, K. R. Brown, P. Maunz, L.-M. Duan, and J. Kim, Phys. Rev. A **89**, 022317 (2014).

[4] L. Jiang, J. M. Taylor, A. S. Sørensen, and M. D. Lukin, Phys. Rev. A **76**, 062323 (2007).

[5] B. K. Malia, Y. Wu, J. Martínez-Rincón, and M. A. Kasevich, Nature **612**, 661 (2022).

[6] A. A. Houck, D. I. Schuster, J. M. Gambetta, J. A. Schreier, B. R. Johnson, J. M. Chow, L. Frunzio, J. Majer, M. H. Devoret, S. M. Girvin, and R. J. Schoelkopf, Nature **449**, 328 (2007).

[7] J.-C. Besse, K. Reuer, M. C. Collodo, A. Wulff, L. Wernli, A. Copetudo, D. Malz, P. Magnard, A. Akin, M. Gabureac, G. J. Norris, J. I. Cirac, A. Wallraff, and C. Eichler, Nature Communications **11**, 4877 (2020).

[8] T. Miyamura, Y. Sunada, Z. Wang, J. Ilves, K. Matsuura, and Y. Nakamura, PRX Quantum **6**, 020347 (2025).

[9] J. O'Sullivan, K. Reuer, A. Grigorev, X. Dai, A. Hernández-Antón, M. H. Muñoz-Arias, C. Hellings, A. Flasby, D. Colao Zanuz, J.-C. Besse, A. Blais, D. Malz, C. Eichler, and A. Wallraff, Nature Communications **16**, 5505 (2025).

[10] Z. Wang, T. Miyamura, Y. Sunada, K. Sunada, J. Ilves, K. Matsuura, and Y. Nakamura, Generation of frequency-bin-encoded dual-rail cluster states via time-frequency multiplexing of microwave photonic qubits (2025), arXiv:2508.10990 [quant-ph].

[11] B. Kannan, A. Almanakly, Y. Sung, A. Di Paolo, D. A. Rower, J. Braumüller, A. Melville, B. M. Niedzielski, A. Karamlou, K. Serniak, A. Vepsäläinen, M. E. Schwartz, J. L. Yoder, R. Winik, J. I.-J. Wang, T. P. Orlando, S. Gustavsson, J. A. Grover, and W. D. Oliver, Nature Physics **19**, 394 (2023).

[12] P. Kurpiers, P. Magnard, T. Walter, B. Royer, M. Pechal, J. Heinsoo, Y. Salathé, A. Akin, S. Storz, J.-C. Besse, S. Gasparinetti, A. Blais, and A. Wallraff, Nature **558**, 264 (2018).

[13] J. Grebel, H. Yan, M.-H. Chou, G. Andersson, C. R. Conner, Y. J. Joshi, J. M. Miller, R. G. Povey, H. Qiao, X. Wu, and A. N. Cleland, Phys. Rev. Lett. **132**, 047001 (2024).

[14] P. Campagne-Ibarcq, E. Zalys-Geller, A. Narla, S. Shankar, P. Reinhold, L. Burkhart, C. Axline, W. Pfaff, L. Frunzio, R. J. Schoelkopf, and M. H. Devoret, Phys. Rev. Lett. **120**, 200501 (2018).

[15] C. J. Axline, L. D. Burkhart, W. Pfaff, M. Zhang, K. Chou, P. Campagne-Ibarcq, P. Reinhold, L. Frunzio, S. M. Girvin, L. Jiang, M. H. Devoret, and R. J. Schoelkopf, Nature Physics **14**, 705 (2018).

[16] A. Almanakly, B. Yankelevich, M. Hays, B. Kannan, R. Assouly, A. Greene, M. Gingras, B. M. Niedzielski, H. Stickler, M. E. Schwartz, K. Serniak, J. I.-J. Wang, T. P. Orlando, S. Gustavsson, J. A. Grover, and W. D. Oliver, Nature Physics **21**, 825 (2025).

[17] A. Narla, S. Shankar, M. Hatridge, Z. Leghtas, K. M. Sliwa, E. Zalys-Geller, S. O. Mundhada, W. Pfaff, L. Frunzio, R. J. Schoelkopf, and M. H. Devoret, Phys. Rev. X **6**, 031036 (2016).

[18] Y.-F. Chen, D. Hover, S. Sendelbach, L. Maurer, S. T. Merkel, E. J. Pritchett, F. K. Wilhelm, and R. McDermott, Phys. Rev. Lett. **107**, 217401 (2011).

[19] K. Koshino, K. Inomata, T. Yamamoto, and Y. Nakamura, Phys. Rev. Lett. **111**, 153601 (2013).

[20] K. Inomata, Z. Lin, K. Koshino, W. D. Oliver, J.-S. Tsai, T. Yamamoto, and Y. Nakamura, Nature Communications **7**, 12303 (2016).

[21] S. Kono, K. Koshino, Y. Tabuchi, A. Noguchi, and Y. Nakamura, Nature Physics **14**, 546 (2018).

[22] J.-C. Besse, S. Gasparinetti, M. C. Collodo, T. Walter, P. Kurpiers, M. Pechal, C. Eichler, and A. Wallraff, Phys. Rev. X **8**, 021003 (2018).

[23] R. Lescanne, S. Deléglise, E. Albertinale, U. Réglade, T. Capelle, E. Ivanov, T. Jacqmin, Z. Leghtas, and E. Flurin, Phys. Rev. X **10**, 021038 (2020).

[24] L. Balembois, J. Travesedo, L. Pallegoix, A. May, E. Bilaud, M. Villiers, D. Estève, D. Vion, P. Bertet, and E. Flurin, Phys. Rev. Appl. **21**, 014043 (2024).

[25] K. Petrovnin, J. Wang, M. Perelshtain, P. Hakonen, and G. S. Paraoanu, PRX Quantum **5**, 020342 (2024).

[26] A. Opremcak, I. V. Pechenezhskiy, C. Howington, B. G. Christensen, M. A. Beck, E. Leonard, J. Suttle, C. Wilen, K. N. Nesterov, G. J. Ribeill, T. Thorbeck, F. Schlenker, M. G. Vavilov, B. L. T. Plourde, and R. McDermott, Science **361**, 1239 (2018).

[27] A. L. Pankratov, A. V. Gordeeva, A. V. Chiginev, L. S. Revin, A. V. Blagodatkin, N. Crescini, and L. S. Kuzmin, Nature Communications **16**, 3457 (2025).

[28] D. L. Campbell, A. Kamal, L. Ranzani, M. Senatore, and M. D. LaHaye, Phys. Rev. Appl. **19**, 064043 (2023).

[29] K. Kubo and H. Goto, Applied Physics Letters **122**, 064001 (2023).

[30] R. Li, K. Kubo, Y. Ho, Z. Yan, Y. Nakamura, and H. Goto, Phys. Rev. X **14**, 041050 (2024).

[31] K. Kubo, Y. Ho, and H. Goto, Phys. Rev. Appl. **22**, 024057 (2024).

[32] W. F. Kindel, M. D. Schroer, and K. W. Lehnert, Phys. Rev. A **93**, 033817 (2016).

[33] P. Forn-Díaz, C. W. Warren, C. W. S. Chang, A. M. Vadiraj, and C. M. Wilson, Phys. Rev. Appl. **8**, 054015 (2017).

[34] A. Blais, A. L. Grimsmo, S. M. Girvin, and A. Wallraff, Rev. Mod. Phys. **93**, 025005 (2021).

[35] A. Yen, Y. Ye, K. Peng, J. Wang, G. Cunningham, M. Gingras, B. M. Niedzielski, H. Stickler, K. Serniak, M. E. Schwartz, and K. P. O'Brien, Phys. Rev. Appl. **23**, 024068 (2025).

[36] D. Esteve, M. H. Devoret, and J. M. Martinis, Phys. Rev. B **34**, 158 (1986).

[37] A. A. Houck, J. A. Schreier, B. R. Johnson, J. M. Chow, J. Koch, J. M. Gambetta, D. I. Schuster, L. Frunzio, M. H. Devoret, S. M. Girvin, and R. J. Schoelkopf, Phys. Rev. Lett. **101**, 080502 (2008).

[38] A. A. Abdumalikov, O. Astafiev, A. M. Zagoskin, Y. A. Pashkin, Y. Nakamura, and J. S. Tsai, Phys. Rev. Lett. **104**, 193601 (2010).

[39] P. Krantz, M. Kjaergaard, F. Yan, T. P. Orlando, S. Gustavsson, and W. D. Oliver, Applied Physics Reviews **6**, 021318 (2019).

[40] C. Eichler, D. Bozyigit, C. Lang, L. Steffen, J. Fink, and A. Wallraff, Phys. Rev. Lett. **106**, 220503 (2011).

[41] C. Eichler, D. Bozyigit, and A. Wallraff, Phys. Rev. A **86**, 032106 (2012).

[42] S. Gasparinetti, M. Pechal, J.-C. Besse, M. Mondal, C. Eichler, and A. Wallraff, Phys. Rev. Lett. **119**, 140504 (2017).

[43] L.-M. Duan, M. D. Lukin, J. I. Cirac, and P. Zoller, Nature **414**, 413 (2001).

[44] S. D. Barrett and P. Kok, Phys. Rev. A **71**, 060310 (2005).

[45] J. Gough and M. R. James, IEEE Transactions on Automatic Control **54**, 2530 (2009).

[46] J. Gough and M. R. James, Communications in Mathematical Physics **287**, 1109–1132 (2008).

[47] J. Combes, J. Kerckhoff, and M. Sarovar, Advances in Physics: X **2**, 784–888 (2017).

[48] L. Luo, D. Hayes, T. Manning, D. Matsukevich, P. Maunz, S. Olmschenk, J. Sterk, and C. Monroe, Fortschritte der Physik **57**, 1133 (2009).

[49] N. Lambert, E. Gigu'ere, P. Menczel, B. Li, P. Hopf, G. Su'arez, M. Gali, J. Lishman, R. Gadhvi, R. Agarwal, A. Galicia, N. Shammah, P. Nation, J. R. Johansson, S. Ahmed, S. Cross, A. Pitchford, and F. Nori, Physics Reports **1153**, 1 (2026).

[50] P. Groszkowski and J. Koch, Quantum **5**, 583 (2021).

[51] X. You, J. A. Sauls, and J. Koch, Phys. Rev. B **99**, 174512 (2019).

[52] U. Vool and M. Devoret, International Journal of Circuit Theory and Applications **45**, 897–934 (2017).

[53] K. Lalumi  re, B. C. Sanders, A. F. van Loo, A. Fedorov, A. Wallraff, and A. Blais, Phys. Rev. A **88**, 043806 (2013).

[54] B. Kannan, D. L. Campbell, F. Vasconcelos, R. Winik, D. K. Kim, M. Kjaergaard, P. Krantz, A. Melville, B. M. Niedzielski, J. L. Yoder, T. P. Orlando, S. Gustavsson, and W. D. Oliver, Science Advances **6**, eabb8780 (2020).